Designing non-heme single atom catalysts for oxygen reduction reaction by high-throughput screening

Y. Kalyanamurthy Sahana and Naiwrit Karmodak*

Department of Chemistry, Shiv Nadar Institution of Eminence, Greater Noida, Delhi-NCR, Uttar Pradesh 201314, India.

E-mail: naiwrit.karmodak@snu.edu.in

Supporting Information

SI: Comparative Analysis: Experimental oxidation potential vs. DFT calculated free energies for Co-Corrole complex

We have benchmarked the accuracy of the revised Perdew–Burke–Ernzerhof (RPBE)[1] exchange-correlation functional, DFT calculations with Hubbard corrections (DFT+U),[2] and Heyd-Scuseria-Ernzerhof (HSE06)[3] hybrid functional against the experimental oxidation potential for water oxidation on Co@cor complex.[4] The HSE06 hybrid functional was employed, combining 25% short-range Hartree–Fock exchange with PBE exchange and correlation, using a range-separation parameter of 0.2 $Å^{-1}$. Figure S1 illustrates a theoretical benchmarking of

the observed potential for Co-corrole for the following reaction:

$$\text{Corrole}-\text{Co}^{\text{III}}-\text{OH} \;\rightarrow\; \text{Corrole}-\text{Co}^{\text{III}}-\text{O} + \text{H}^{+} + \text{e}^{-} \tag{1}$$

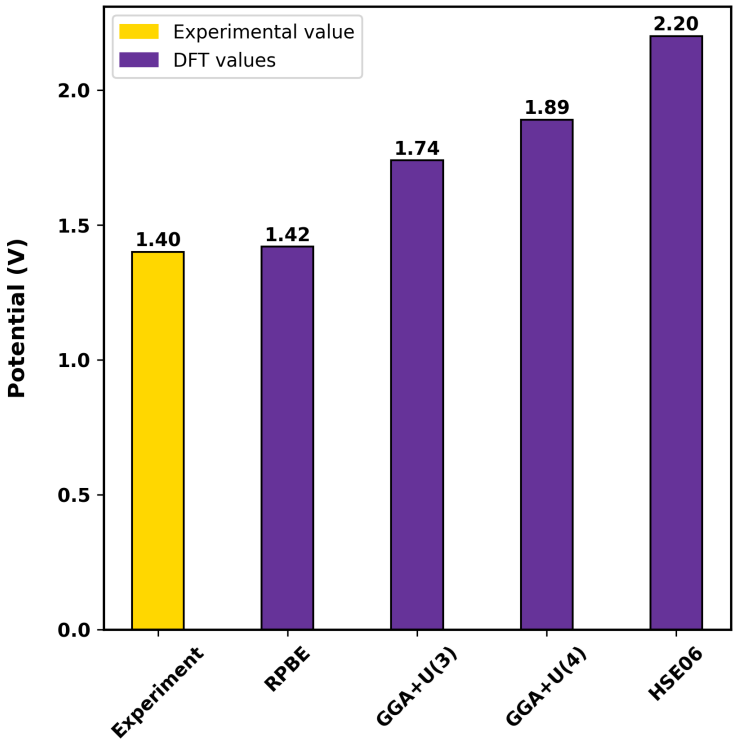

Figure S 1: Comparison of experimental and DFT-calculated redox potentials for Co–corrole oxidation.

The experimentally observed potential for this redox reaction is 1.40 V.[4] Using the RPBE, we obtain an oxidation potential of 1.42 V, which agrees well with the experimental result. However, incorporating Hubbard corrections (GGA+U(3) where U=3, and GGA+U(4) where U=4 and the HSE06 hybrid functional, the calculated potential progressively increases. Based on this trend, we have used the RPBE functional to perform high-throughput screening of non-heme single-atom catalysts (SACs) for ORR.

We have performed additional benchmark studies to assess the applicability of the GGA and GGA+U approaches, as the Hubbard U parameter is known to influence adsorption energetics on 3d transition-metal SACs strongly. A representative set of 21 SACs containing

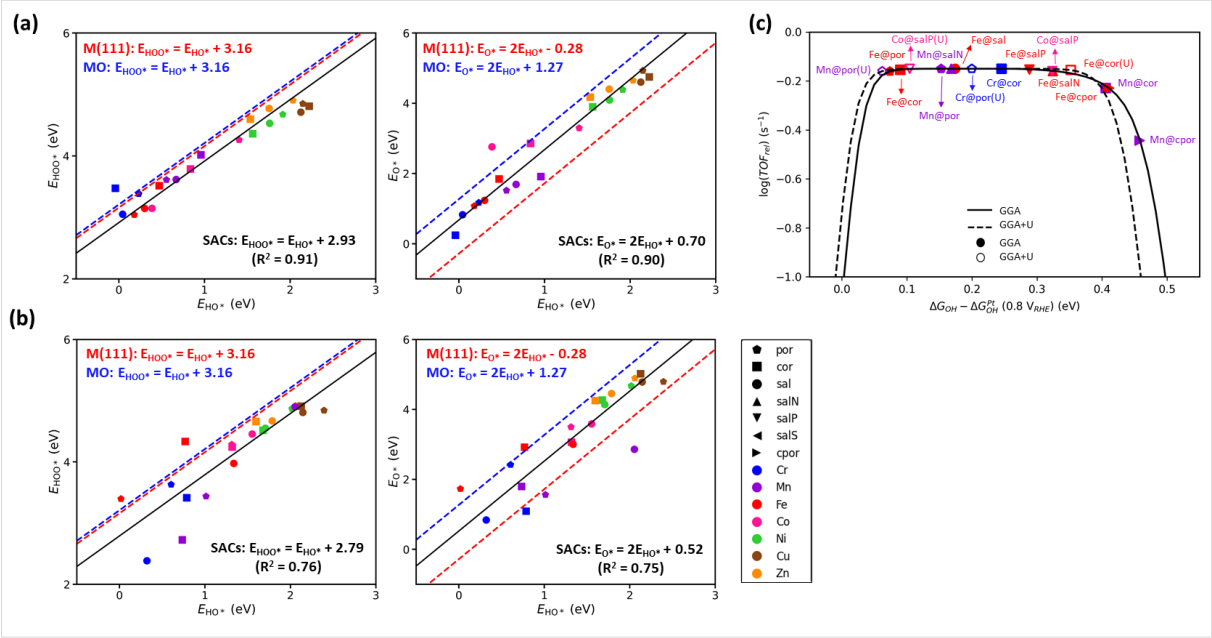

Figure S 2: Scaling relations (black line) between adsorption energies of HO* vs. HOO* and HO* vs. O* intermediates (in eV) with (a) GGA and (b) GGA+U functional on the SACs without graphene support. Comparisons are made with scaling lines obtained previously for metal (111) surfaces (red line) and metal oxide surfaces (blue line).[5] The details of the linear fits are provided with R^2 values. (c) Microkinetic modeling of the 4e$^-$ pathway for SACs on graphene support using GGA and GGA+U functional. The legend indicates the color codes and markers corresponding to different SACs.

Cr, Mn, Fe, Co, Ni, Cu, and Zn in porphyrin, corrole, and salen coordination environments is selected. The U values in Table S1 are adopted from Ref. (6). To isolate intrinsic functional effects, scaling relations are established without the graphene support.

Table S 1: The values of U (in eV) for selected 3d transition-metal elements.[6]

3d	Cr	Mn	Fe	Co	Ni	Cu	Zn
U(eV)	2.79	3.06	3.29	3.42	3.40	3.87	4.12

Figure S2a and S2b show the HO* vs. HOO* and HO* vs. O* scaling relations obtained using GGA and GGA+U functionals. For HO* vs. HOO*, the intercepts are 2.93 eV (GGA) and 2.79 eV (GGA+U), while for HO* vs. O*, the intercepts are 0.70 and 0.52 eV, respectively, indicating good agreement between the two methods. In both cases, linear scaling relations are preserved across different metals and coordination environments.

Although GGA+U maintains comparable intercepts, it introduces greater scatter around the scaling lines, particularly in the $\Delta G_{\mathrm{HO}*}$ descriptor that governs ORR activity in this work. In contrast, RPBE yields tighter correlations and more systematic trends, enabling more reliable descriptor-based analysis and consistent activity ranking.

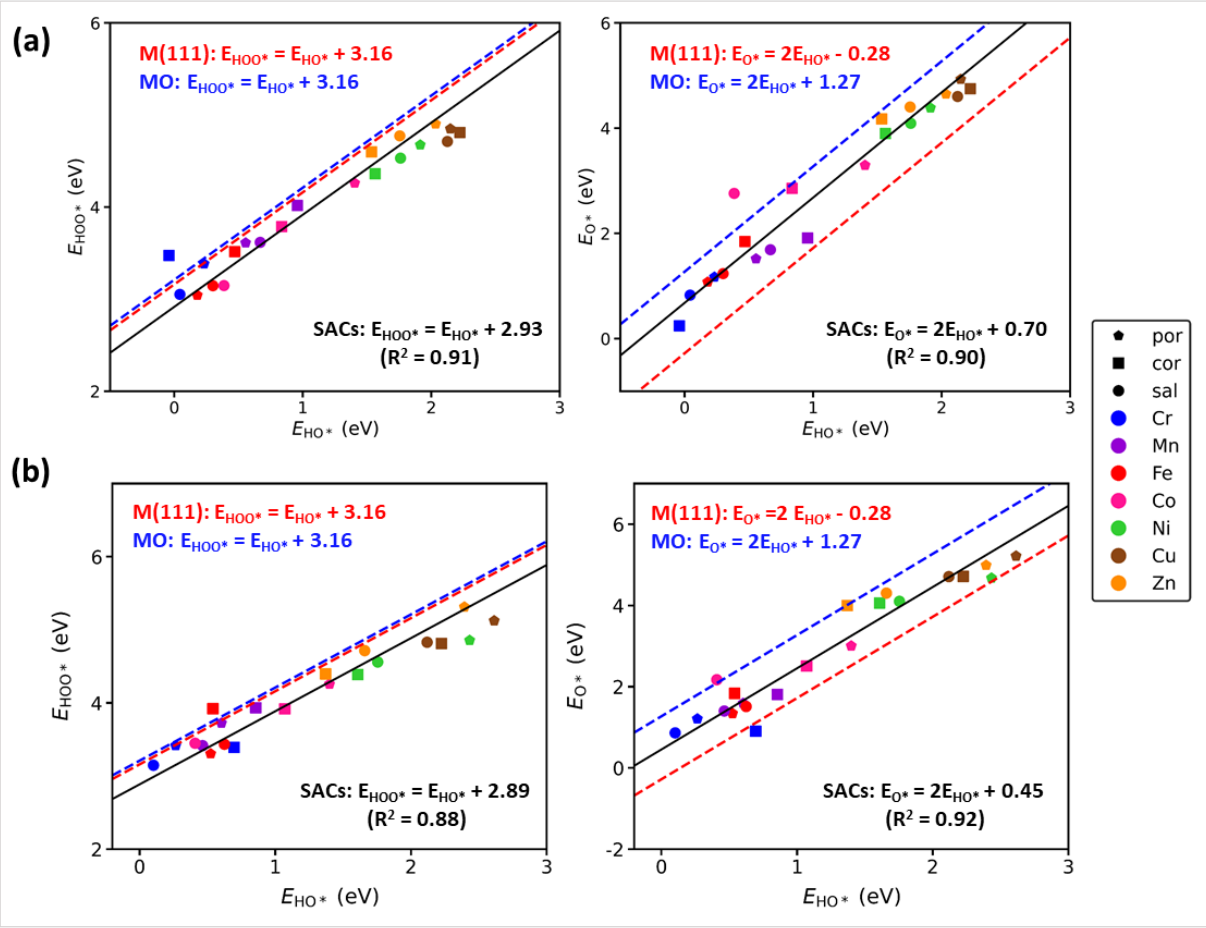

Figure S 3: Scaling relations between adsorption energies of HO* vs. HOO* and HO* vs. O* on SACs (a) without graphene and (b) with graphene as support using RPBE functional.

SII: Formation free energy calculations of the SACs

The formation energies are calculated to understand the stability of the metal complexes on the heme and non-heme frameworks adsorbed on the graphene support. The formation energy (ΔE_{form}) is composed of two different energy terms, ΔE_1 and ΔE_2. ΔE_1 corresponds to the formation of the SACs (M@mac) from the stable references for the macrocyclic framework (mac) and the metal atoms (M), as shown in Equation (3). ΔE_2 denotes the adsorption energy of the SACs on the graphene support (Equation 4).

$$\Delta E_{\text{form}} = \Delta E_1 + \Delta E_2 \tag{2}$$

$$\Delta E_1 = E_{\text{M@mac}} - E_{\text{mac}} - E_{\text{M}} + nE_{\text{H}_2} \tag{3}$$

$$\Delta E_2 = E_{\text{M@mac-graphene}} - E_{\text{M@mac}} - E_{\text{graphene}} \tag{4}$$

In these equations, $E_{\text{M@mac-graphene}}$ denotes the DFT-calculated energy of the adsorbed complexes on the graphene surface, $E_{\text{M@mac}}$ and E_{graphene} denotes the DFT energies of the macrocyclic complexes without the graphene surface and the pristine graphene surface, respectively. E_M corresponds to metal atom references (here we have considered the bulk metal), and E_{H_2} is the DFT-calculated gaseous H_2 molecular energy. Since the macrocyclic framework is satisfied with attached H atoms, after complexation with the metal dopants, the attached H is assumed to be removed as molecular H_2 to satisfy the reaction stoichiometry.[7,8]

SIII: Reaction free energy calculations

The reaction energetics are obtained by calculating the thermodynamic free energies of the different intermediates using the computational hydrogen electrode (CHE) method.[9,10] Electronic binding energies (E_{ads}) for the adsorbed intermediates are determined relative to the total energies of gaseous H_2, H_2O, and adsorbed H_2O molecules.[11–13] The proposed mech-

anism for the $4e^-$ pathway includes O_2 adsorption in the initial step at the catalytic site, followed by the PCET steps resulting in HOO*, O*, and HO* intermediates (Equations (5) to (11)). The $2e^-$ pathway resulting in the formation H_2O_2, follows Equations (5) to (7) and Equations (12) and (13).

$$O_2(g) \longrightarrow O_2(dl) \tag{5}$$

$$O_2(dl) + {}^* \longrightarrow O_2^* \tag{6}$$

$$O_2^* + H^+ + e^- \longrightarrow HOO^* \tag{7}$$

$$HOO^* + H^+ + e^- \longrightarrow O^* + H_2O(l) \tag{8}$$

$$O^* + H^+ + e^- \longrightarrow HO^* \tag{9}$$

$$HO^* + H^+ + e^- \longrightarrow H_2O^* \tag{10}$$

$$H_2O^* \longrightarrow H_2O(l) + {}^* \tag{11}$$

$$HOO^* + H^+ + e^- \longrightarrow H_2O_2^* \tag{12}$$

$$H_2O_2^* \longrightarrow H_2O_2(aq) + {}^* \tag{13}$$

The adsorption energies of each of the reaction intermediates are calculated employing the following equations:

$$E_{O_2} = E_{\text{slab-}O_2^*} - E_{\text{slab}} - 2E_{H_2O^*} + 2E_{H_2} \tag{14}$$

$$E_{HOO^*} = E_{\text{slab-}HOO^*} - E_{\text{slab}} - E_{H_2O^*} - E_{H_2O} + \tfrac{3}{2}E_{H_2} \tag{15}$$

$$E_{HO^*} = E_{\text{slab-}HO^*} - E_{\text{slab}} - E_{H_2O^*} + \tfrac{1}{2}E_{H_2} \tag{16}$$

$$E_{O^*} = E_{\text{slab-}O^*} - E_{\text{slab}} - E_{H_2O^*} + E_{H_2} \tag{17}$$

In these formulations, $E_{\text{slab-ads}^*}$ denotes the energy of the surface with the adsorbate attached, and E_{slab} signifies the energy of the pristine slab surface. $E_{H_2O^*}$ and E_{H_2O} represent the energy

of the H_2O molecule adsorbed on the catalyst surface and in the gas phase, respectively. E_{H_2} is the energy of a gaseous H_2 molecule. The binding free energies ΔG_{ads*} for all adsorbates on the catalysts are computed by the addition of zero-point energy (ΔZPE) and entropy ($T\Delta S$) corrections, as expressed by Equation (18) at room temperature.[9]

$$\Delta G_{ads} = E_{ads} + \Delta ZPE - T\Delta S \tag{18}$$

Previous studies have shown that the dissociative reduction pathway of O_2 is unlikely on many catalyst surfaces because of the high energy barrier associated with O–O bond cleavage.[9,14] Accordingly, in this study, we consider the associative pathway (Equation 7) to be the most feasible mechanism for O_2 reduction on the SACs.

SIV: Microkinetic modeling of the ORR

The microkinetic simulations are performed using the CatMAP package.[15–17] Steady-state surface coverages of adsorbed species are obtained using the steady-state approximation. The rates of elementary reactions are computed using the expression:

$$\text{Rate} = k_f \prod \theta_{\text{reactants}} - k_r \prod \theta_{\text{products}} \tag{19}$$

Here, θ denotes the surface coverage of each intermediate. The forward and reverse rate constants (k_f and k_r) are calculated via transition state theory:

$$k = A \cdot \exp\left(-\frac{G^{\ddagger}}{k_B T}\right) \tag{20}$$

Here, A is the pre-exponential factor (s^{-1}), $G^{\ddagger}$ is the activation free energy, k_B is the Boltzmann constant, and T is the temperature (298.15 K).

Elementary steps considered in this framework include oxygen diffusion from the gas

phase to the electrochemical double layer, surface adsorption, and a series of proton-coupled electron transfer (PCET) steps. The diffusion of O_2 from the bulk aqueous phase to the double layer is modeled as a chemical step with a fixed rate constant of 8×10^5 s^{-1}, consistent with a rotating disk electrode at 1600 rpm.[15] The adsorption of O_2 and the desorption of H_2O_2 are assigned prefactors of 1×10^8 s^{-1} to account for solvent reorganization at the interface.[16] The PCET steps are modeled using the computational hydrogen electrode (CHE) approach, wherein the chemical potential of a proton–electron pair is referenced to half the energy of a H_2 molecule in the gas phase.

The adsorption of reaction intermediates can induce pronounced local structural, electronic, and dynamic effects that may, in principle, lead to deviations from constant PCET activation barriers. To account for this, we do not apply a constant barrier to all elementary steps. In particular, the O–O bond cleavage step (*HOO + H^+ + e^- → *O + H_2O), which involves substantial bond rearrangement, is treated explicitly using a descriptor-based activation barrier derived from a linear scaling relation between the transition-state free energy and the free-energy difference of the *O and *HOO intermediates. This step has been identified as the kinetically most critical step in a recent study by Zhang *et al.* on porphyrin-based single-atom catalysts and is therefore expected to govern the overall ORR rate trend.[18] Specifically, a linear scaling relation was established to predict the transition-state energy for O–O bond cleavage on SACs based on the free-energy difference between *O and *HOO intermediates, yielding the activation barrier G_a as expressed below.[18]

$$E_a = 0.86\,(G_{O^*} - G_{HOO^*}) + 1.86 \tag{21}$$

The reliability of the microkinetic model employing a descriptor-dependent activation barrier for the O–O The bond cleavage step and constant intrinsic barriers for the remaining PCET steps have been previously assessed by Zhang et al. through a comparison of experimentally measured and theoretically predicted onset potentials. The resulting linear correlation and quantitative agreement indicate that, despite the inherent approximations

in the treatment of activation barriers and solvent effects, the microkinetic framework is capable of reliably capturing relative ORR activity trends on porphyrin-based single-atom catalysts.[18]

We have used a similar relation to determine the O-O bond breaking transition barrier in this study for the HOO* intermediate. All other PCET steps not involving bond breaking are assigned a constant intrinsic barrier of 0.26 eV, assuming a symmetric transition state with a charge transfer coefficient of 0.5.[15] A prefactor of 1×10^9 s^{-1} is used for all PCET steps to account for solvent reorganization and interfacial charge dynamics.[16] Free energies of all species are referenced from the scaling relations shown in Figure 2 and are corrected for the RHE potential. The energy of O_2 in both gaseous and double-layer phases is set to 5.19 eV at 0 V_{RHE}.[16,19] The mole fraction of O_2 is fixed at 2.34×10^{-5}, corresponding to 1 atm O_2 in equilibrium with water.

Assuming the steady state approximation, we have

$$\theta_* + \theta_{O_2{}^*} + \theta_{HOO^*} + \theta_{O^*} + \theta_{HO^*} + \theta_{H_2O^*} = 1 \tag{22}$$

The rates of elementary reactions are computed using the expression:

$$\text{Rate} = k_f \prod \theta_{\text{reactants}} - k_r \prod \theta_{\text{products}} \tag{23}$$

Here, θ denotes the surface coverage of each intermediate. The forward and reverse rate constants (k_f and k_r) are calculated via transition state theory:

$$k = A \cdot \exp\left(-\frac{G^\ddagger}{k_B T}\right) \tag{24}$$

Here, A is the pre-exponential factor (s^{-1}), $G^\ddagger$ is the activation free energy, k_B is the Boltz-

mann constant, and T is the temperature (298.15 K).

$$r_1 = k_{f1}\theta_* p_{\mathrm{O_2}} - k_{r1}\theta_{\mathrm{O_2}^*} \tag{25}$$

$$r_2 = k_{f2}\theta_{\mathrm{O_2}^*} - k_{r2}\theta_{\mathrm{HOO}^*} \tag{26}$$

$$r_3 = k_{f3}\theta_{\mathrm{HOO}^*} - k_{r3}\theta_{\mathrm{O}^*} p_{\mathrm{H_2O}} \tag{27}$$

$$r_4 = k_{f4}\theta_{\mathrm{O}^*} - k_{r4}\theta_{\mathrm{HO}^*} \tag{28}$$

$$r_5 = k_{f5}\theta_{\mathrm{HO}^*} - k_{r5}\theta_{\mathrm{H_2O}^*} \tag{29}$$

$$r_6 = k_{f6}\theta_{\mathrm{H_2O}^*} - k_{r6}\theta_* p_{\mathrm{H_2O}} \tag{30}$$

For the fast reaction steps, the rate (r_i, i corresponding to 1, 2, 4, 5, and 6) will be denoted as below, while having the steady state approximation.

$$r_1 = 0 \; ; \; r_2 = 0 \; ; \; r_4 = 0 \; ; \; r_5 = 0 \; ; \; r_6 = 0 \tag{31}$$

The rate of O_2 reduction will be given by the O-O bond cleavage step as below:

$$rate = \frac{d[HOO^*]}{dt} = k_{f3}\theta_{\mathrm{HOO}^*} \tag{32}$$

The coverage of θ_{HOO^*} can be obtained using 25, 26, and 31 as:

$$\theta_{\mathrm{HOO}^*} = K_1 K_2 p_{\mathrm{O_2}} \tag{33}$$

Here, K_1 and K_2 correspond to the equilibrium constant of the first and the second reaction step, as denoted by $\frac{k_{f1}}{k_{r1}}$, and $\frac{k_{f2}}{k_{r2}}$, respectively. $p_{\mathrm{O_2}}$ corresponds to the partial pressure of O_2. This shows that the partial pressure of gaseous O_2 predominantly determines the rate of the reaction.

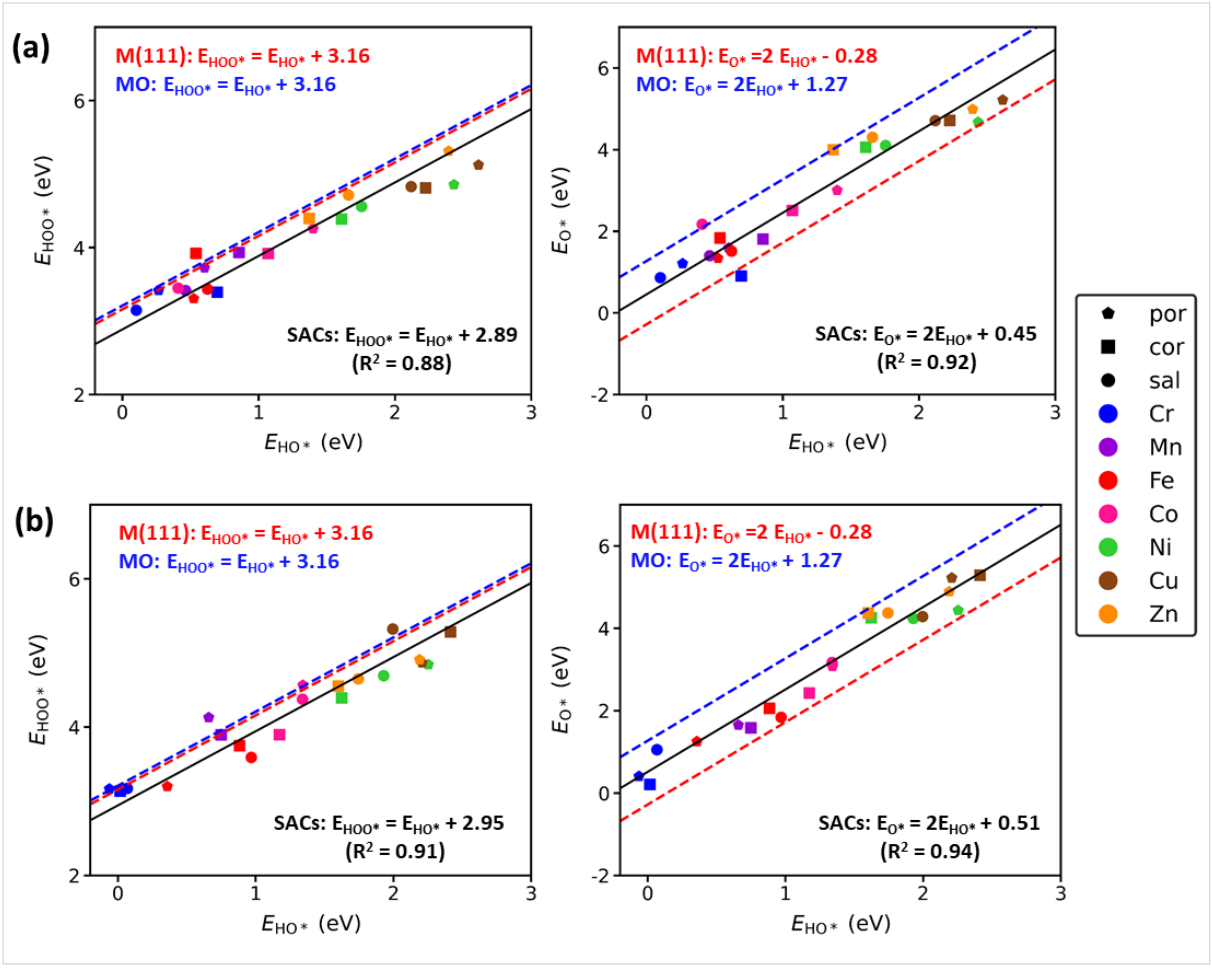

Figure S 4: Scaling relations (black line) between adsorption energies of HO* vs. HOO* and HO* vs. O* intermediates (in eV) with (a) implicit solvent and (b) explicit solvent models on the SACs with graphene support. Comparisons are made with scaling lines obtained previously for metal (111) surfaces (red line) and metal oxide surfaces (blue line).[5]

To elucidate the effect of the solvent, we compare the scaling relations obtained with implicit and explicit solvent interactions. In a previous study with SACs, the influence of explicit water molecules on the adsorption energies of O*, HOO*, HO*, and O_2^* has been investigated by varying the number of surrounding water molecules and averaging over different solvation configurations.[18] Across these solvation environments, explicit solvent-induced corrections of approximately 0.05, 0.35, and 0.40 eV are identified for O, HO*, and HOO*, respectively. Using these corrections, we have plotted the scaling relations between the ORR intermediates as shown in Figures S4a and S4b. Notably, the inclusion of explicit

solvent effects leads to only minor variations in the intercept values of the scaling relations.

SV: Stability Pourbaix diagram

One of the defining features of an effective ORR catalyst is its resistance to degradation under aqueous electrochemical conditions.[8] As a subsequent screening step, the electrochemical stability of the catalysts is evaluated across a range of pH values and applied potentials.[20–23] As part of the demetallation mechanism, SACs undergo protonation and potential hydrogenation of the surrounding nitrogen ligands, which can ultimately lead to the demetallation of the embedded metal ion into the aqueous medium. The demetallation reaction is described by the following equation:

$$C_xN_yMO_aH_b + (2\,a - b + m)H^+ \longrightarrow C_xN_yH_m + M^{q+} + aH_2O + (q + 2\,a + b - m)e^- \tag{34}$$

To evaluate the impact of the electrochemical environment, we compute the dissolution free energies, $\Delta G_{\mathrm{pbx}}(E, \mathrm{pH})$ which represent the thermodynamic stability of the catalysts with respect to their dissolution into the most stable ionic, molecular, elemental, or solid forms at a given electrode potential and pH. These dissolution free energies of the M@SACs are then calculated for constructing the pH vs. potential Pourbaix diagrams. From the Materials Project database,[24] ionic reference energies for the required aqueous cations are collected at the corresponding pH and potential. Gibbs energies for the demallation are calculated using the Nernst equation as a function of pH (1-14) and applied potential (0-1.0 V_{SHE}). Thermodynamic corrections are applied for the intermediates O* and HO*.[9] Among the bare slab, HO*-covered slab, and O*-covered slab, the lowest-energy dissolution pathway is chosen for each pH and potential grid point.

To construct the Pourbaix stability of the materials, the demetallation free energy values are computed using Equation (35) at different applied voltages and free energy values. Based on methods reported by Persson *et al.*,[25] and Singh *et al.*,[21] the Pourbaix Gibbs free energy

($\Delta G_{pbx}(C, \mathrm{pH}, E)$) for solvated metal ions at an applied potential and solvent pH is calculated as follows:

$$\Delta G_{\mathrm{pbx}}(C,\ \mathrm{pH},\ E) = \Delta G^0 + 0.059 \log C - n\mu_{\mathrm{H_2O}} + 0.059\,(n_{\mathrm{H}} - 2n_{\mathrm{O}})\,\mathrm{pH} + (-n_{\mathrm{H}} + 2n_{\mathrm{O}} + q)\,E \tag{35}$$

In this case, C stands for the concentration of the ionic species. n_{H} and n_{O} represent the number of hydrogen and oxygen atoms, respectively. The formation energy of water, $\mu_{\mathrm{H_2O}}$, is set to the experimental value of -2.46 eV. q represents the charge of the metal ions formed after demetallation from the SAC. To calculate the reference standard free energies (ΔG^0), we have used the DFT calculated free energy of the SACs with the different adsorbed oxygenated intermediates, the SAC without the adsorbate, and the SACs after demetallation. The free energy values of the solvated ionic species formed after dematallation of the ions are obtained from the different Pourbaix data repositories.[26–28] 10^{-6} M is the estimated concentration of the aqueous species.

SVI: Electric field and pH-dependent modeling

In recent studies, modulating the electric field has provided an accurate strategy for quantifying the effect of solvent pH on the electrocatalytic activity of SACs for ORR.[29,30] This approach enables coupling the pH modulation effect to the microkinetic modeling pathways. To replicate pH dependence on the reaction energetics, electric fields are applied by a saw-tooth potential profile using the Quantum Espresso package.[31] The RPBE functional is used with an energy cutoff of 40 Ry and a density cutoff of 400 Ry. We have used a similar calculation method as reported in the references[29,30] to incorporate the effect of the electric field in the adsorption energies. In the previous studies, defining the electric field by varying the strengths has accurately captured the effect of the solvent pH on the intermediate adsorption energies and shows a good correlation to the experimental activity trends. The calculations are performed, with the electronic self-consistency cycle converged to within

1×10^{-6} Ry for each step with the force convergence threshold set to 0.05 eV Å^{-1}. After the adsorbate geometries are completely optimized for each field strength, the conformation with the lowest energy is utilized for further energy analysis. Both SHE and RHE potentials are taken into account when correcting the calculated adsorption energies. The calculations are performed, with the electronic self-consistency cycle converged to within 1×10^{-6} Ry for each step with the force convergence threshold set to 0.05 eV Å^{-1}. After the adsorbate geometries are completely optimized for each field strength, the conformation with the lowest energy is utilized for further energy analysis. Both SHE and RHE potentials are taken into account when correcting the calculated adsorption energies.

A parallel-plate capacitor model is applied to calculate the electric field corresponding to a specific potential vs. SHE:

$$\vec{E} = \frac{\sigma}{\varepsilon\varepsilon_0} = \frac{C_H(U_{\mathrm{SHE}} - U_{\mathrm{PZC}})}{\varepsilon\varepsilon_0} \tag{36}$$

Here, ε_0 represents the vacuum permittivity (8.85×10^{-12} F m^{-1}), ε stands for the relative dielectric constant of water close to the interface, which is equal to 2,[32] and C_H is the Helmholtz capacitance (presumed to be constant at 25 μF cm^{-2} for all surfaces).[16] The potential vs. SHE is represented by U_{SHE}, and the potential at the point of zero charge is represented by U_{PZC}. Following Trasatti *et al.*, U_{PZC} is calculated from work function (ϕ) in ion-free water using the following equation:[33]

$$\phi = eU_{\mathrm{PZC}} + \phi_{\mathrm{SHE}} \tag{37}$$

ϕ_{SHE} denotes the absolute potential of SHE. Although reported values of ϕ_{SHE} vary between 4.3 and 4.8 eV depending on experimental conditions, in this work we adopted the IUPAC recommended value of 4.44 eV. We have set the bulk dielectric constant of the solvent to 78.3, corresponding to water at 300 K, to determine the PZCs. The dielectric cavity is defined with a filling threshold of 0.7. To evaluate the reaction of adsorbates to external electric

fields, a second-order polynomial is fitted to the predicted binding energies of adsorbates over the whole range of applied fields. From these fits, the intrinsic dipole moment (μ) and polarizability (α) for every material are determined using:

$$\Delta G_{\text{ads}} = \Delta G_{\text{ads}}^{\text{PZC}} + \mu\vec{E} - \tfrac{1}{2}\alpha\vec{E}^2 \tag{38}$$

where $\Delta G_{\text{ads}}^{\text{PZC}}$ is the adsorption energy at the PZC, i.e., without an applied field. To determine values of μ and α, we have applied an electric field varying between -0.4 and 0.4 V Å^{-1}. All corrections to the free energy of adsorption at U_{RHE} are reflected in the final expression, as follows:

$$\Delta G_{\text{ads}} = \Delta G_{\text{ads}}^{\text{PZC}} - \mu\vec{E} - \frac{\alpha}{2}\vec{E}^2 - neU_{\text{RHE}} \tag{39}$$

This equation accounts for changes in adsorption energy resulting from both the field and potential. The local electric field experienced at the interface varies substantially with pH, even with constant RHE potential, given that the disparity between U_{RHE} and U_{SHE} is directly correlated with pH ($U_{\text{RHE}} = U_{\text{SHE}} + 0.059\text{pH}$).

We have used the computed electric field to determine the field-dependent binding energies for each adsorbate as shown in Equation (38). Although this method uses predefined experimental values for Helmholtz capacitance (C_H) and PZC (U_{PZC}), it efficiently corrects the binding energies considering the electrostatic terms. In recent studies, this approach has been found to effectively define the pH effects on the binding energies of the reaction intermediates and align well with the experiments.[29,30]

$$G_{\text{ads}}(U_{\text{RHE}}) = G_{\text{ads}}(U = 0) - neU_{\text{RHE}} \tag{40}$$

n is the number of electrons and e is the charge.

To quantify the shift of adsorption free energies, $G_{\text{ads}} - G_{\text{ads}}^{\text{PZC}}$, caused by an external

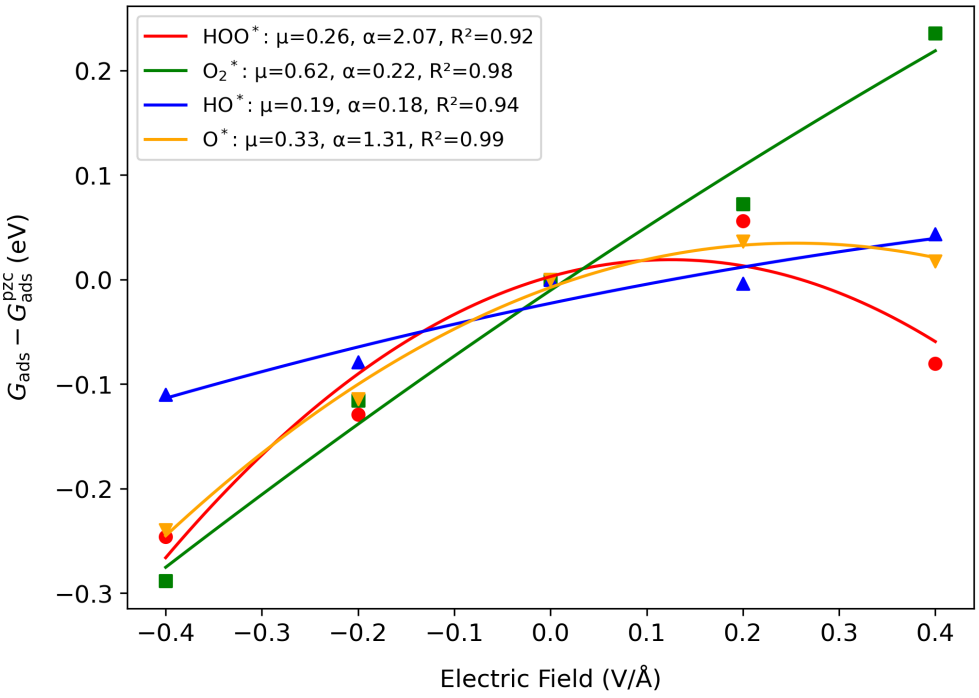

Figure S 5: Effect of the applied electric field on the adsorption energies of ORR intermediates on Fe@sal.

interfacial field ($\vec{E}$) (Figure S5), we have fitted the field response to a dipole-polarizability form. The first order (μ) term represents the interaction between the field and the net interfacial dipole of the adsorbate. In contrast, the second-order (α) term represents the redistribution of charges caused by the field. HOO* has the highest curvature ($\alpha = 2.07$) and the smallest linear component ($\mu = 0.26$) of the four intermediates. This is consistent with the convex trend in $G_{\text{ads}} - G_{\text{ads}}^{\text{PZC}}$ and indicates that the thermodynamic binding of HOO* is highly sensitive to the field magnitude, stabilizing at small positive fields but decreasing again as the field grows. O_2^* has a small polarizability ($\alpha = 0.22$) and the largest dipolar response ($\mu = 0.62$). $G_{\text{ads}} - G_{\text{ads}}^{\text{PZC}}$ increases almost linearly with the field, suggesting that the direction of the field largely governs the thermodynamics of molecule O_2 binding. The field sensitivity of HO* is the weakest overall ($\mu = 0.19$, $\alpha = 0.18$). Over the range under study, $G_{\text{ads}} - G_{\text{ads}}^{\text{PZC}}$ fluctuates gradually and almost linearly, suggesting a stronger binding motif with little reorganization under the field. Both μ and α show moderate values for O*

($\mu = 0.33$, $\alpha = 1.31$). At low positive fields, O* becomes significantly more stable before the trend flattens, indicating clear curvature in the free-energy curve.

SVII: Scaling Relations among ORR Intermediates

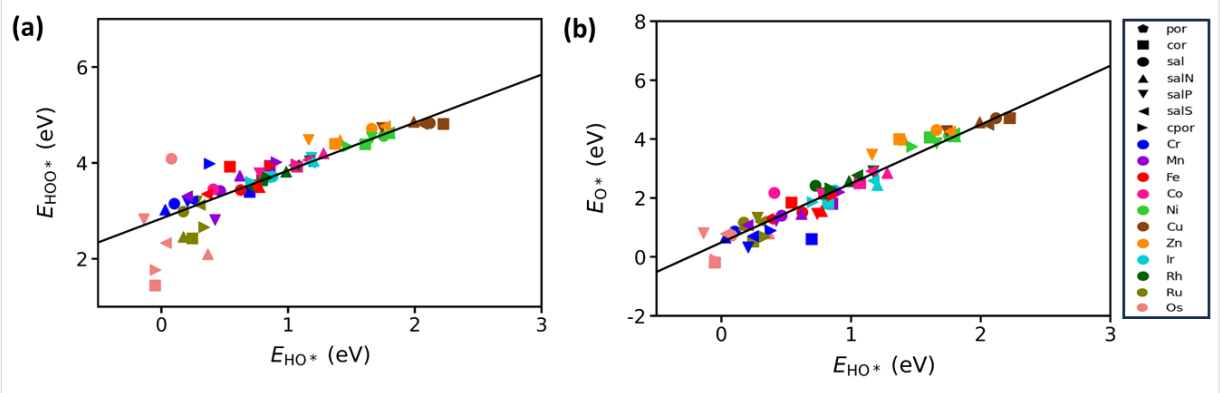

Figure S 6: Scaling relations between adsorption energies of (a) HO* vs. HOO* and (b) HO* vs. O* including all SACs considered in this study. Os and Ru exhibit considerable deviations in the HOO* vs. HO* relation due to their stronger binding affinity for the HO* intermediate.

References

(1) Hammer, B.; Hansen, L. B.; Nørskov, J. K. Improved adsorption energetics within density-functional theory using revised Perdew-Burke-Ernzerhof functionals. *Phys. Rev. B.* **1999**, *59*, 7413.

(2) Himmetoglu, B.; Floris, A.; De Gironcoli, S.; Cococcioni, M. Hubbard-corrected DFT energy functionals: The LDA+ U description of correlated systems. *Int. J. Quantum Chem.* **2014**, *114*, 14–49.

(3) Heyd, J.; Scuseria, G. E.; Ernzerhof, M. Hybrid functionals based on a screened Coulomb potential. *J. Chem. Phy* **2003**, *118*, 8207–8215.

(4) Mondal, B.; Chattopadhyay, S.; Dey, S.; Mahammed, A.; Mittra, K.; Rana, A.; Gross, Z.; Dey, A. Elucidation of factors that govern the 2e–/2H+ vs 4e–/4H+ selectivity of water oxidation by a cobalt corrole. *J. Am. Chem. Soc.* **2020**, *142*, 21040–21049.

(5) Li, H.; Kelly, S.; Guevarra, D.; Wang, Z.; Wang, Y.; Haber, J. A.; Anand, M.; Gunasooriya, G. K. K.; Abraham, C. S.; Vijay, S.; et al. Analysis of the limitations in the oxygen reduction activity of transition metal oxide surfaces. *Nat. Catal.* **2021**, *4*, 463–468.

(6) Lin, C.-Y.; Zhang, L.; Zhao, Z.; Xia, Z. Design principles for covalent organic frameworks as efficient electrocatalysts in clean energy conversion and green oxidizer production. *Adv. Mater.* **2017**, *29*, 1606635.

(7) Holby, E. F.; Wang, G.; Zelenay, P. Acid stability and demetalation of PGM-free ORR electrocatalyst structures from density functional theory: a model for "single-atom catalyst" dissolution. *ACS Catal.* **2020**, *10*, 14527–14539.

(8) Helsel, N.; Choudhury, P. Enhancing the Stability of a Pt-Free ORR Catalyst via Reaction Intermediates. *Adv. Mater. Interfaces* **2023**, *10*, 2202132.

(9) Nørskov, J. K.; Rossmeisl, J.; Logadottir, A.; Lindqvist, L.; Kitchin, J. R.; Bligaard, T.; Jonsson, H. Origin of the overpotential for oxygen reduction at a fuel-cell cathode. *J. Phys. Chem. B* **2004**, *108*, 17886–17892.

(10) Singh, S.; Bononi, F.; Andreussi, O.; Karmodak, N. Thermodynamic and kinetic modeling of electrocatalytic reactions using a first-principles approach. *J. Chem. Phys.* **2023**, *159*.

(11) Liu, S.; White, M. G.; Liu, P. Mechanism of oxygen reduction reaction on Pt (111) in alkaline solution: importance of chemisorbed water on surface. *J. Phys. Chem. C* **2016**, *120*, 15288–15298.

(12) Liu, S.; White, M. G.; Liu, P. Oxygen reduction reaction on ag (111) in alkaline solution: A combined density functional theory and kinetic monte carlo study. *ChemCatChem* **2018**, *10*, 540–549.

(13) Dickens, C. F.; Kirk, C.; Nørskov, J. K. Insights into the electrochemical oxygen evolution reaction with ab initio calculations and microkinetic modeling: beyond the limiting potential volcano. *J. Phys. Chem. C* **2019**, *123*, 18960–18977.

(14) Kulkarni, A.; Siahrostami, S.; Patel, A.; Nørskov, J. K. Understanding catalytic activity trends in the oxygen reduction reaction. *Chem. Rev.* **2018**, *118*, 2302–2312.

(15) Hansen, H. A.; Viswanathan, V.; Nørskov, J. K. Unifying kinetic and thermodynamic analysis of 2 e–and 4 e–reduction of oxygen on metal surfaces. *J. Phys. Chem. C* **2014**, *118*, 6706–6718.

(16) Kelly, S. R.; Kirk, C.; Chan, K.; Nørskov, J. K. Electric field effects in oxygen reduction kinetics: rationalizing pH dependence at the Pt (111), Au (111), and Au (100) electrodes. *J. Phys. Chem. C* **2020**, *124*, 14581–14591.

(17) Medford, A. J.; Shi, C.; Hoffmann, M. J.; Lausche, A. C.; Fitzgibbon, S. R.; Bligaard, T.; Nørskov, J. K. CatMAP: a software package for descriptor-based microkinetic mapping of catalytic trends. *Catal. Lett.* **2015**, *145*, 794–807.

(18) Zhang, D.; She, F.; Chen, J.; Wei, L.; Li, H. Why Do Weak-Binding M–N–C Single-Atom Catalysts Possess Anomalously High Oxygen Reduction Activity? *J. Am. Chem. Soc.* **2025**, *147*, 6076–6086.

(19) Viswanathan, V.; Hansen, H. A.; Rossmeisl, J.; Nørskov, J. K. Unifying the 2e–and 4e–reduction of oxygen on metal surfaces. *J. Phys. Chem. Lett.* **2012**, *3*, 2948–2951.

(20) Jain, A.; Wang, Z.; Nørskov, J. K. Stable two-dimensional materials for oxygen reduction and oxygen evolution reactions. *ACS Energy Lett.* **2019**, *4*, 1410–1411.

(21) Singh, A. K.; Zhou, L.; Shinde, A.; Suram, S. K.; Montoya, J. H.; Winston, D.; Gregoire, J. M.; Persson, K. A. Electrochemical stability of metastable materials. *Chem. Mater.* **2017**, *29*, 10159–10167.

(22) Karmodak, N.; Andreussi, O. Catalytic activity and stability of two-dimensional materials for the hydrogen evolution reaction. *ACS Energy Lett.* **2020**, *5*, 885–891.

(23) Karmodak, N.; Nørskov, J. K. Activity And Stability of Single-And Di-Atom Catalysts for the O2 Reduction Reaction. *Angew. Chem. Int. Ed.* **2023**, *62*, e202311113.

(24) Jain, A.; Ong, S. P.; Hautier, G.; Chen, W.; Richards, W. D.; Dacek, S.; Cholia, S.; Gunter, D.; Skinner, D.; Ceder, G.; et al. Commentary: The Materials Project: A materials genome approach to accelerating materials innovation. *APL Mater.* **2013**, *1*.

(25) Persson, K. A.; Waldwick, B.; Lazic, P.; Ceder, G. Prediction of solid-aqueous equilibria: Scheme to combine first-principles calculations of solids with experimental aqueous states. *Phys. Rev. B* **2012**, *85*, 235438.

(26) Pourbaix, M. Atlas of electrochemical equilibria in aqueous solutions. *NACE* **1966**,

(27) Takeno, N. Atlas of Eh-pH diagrams. *Geological survey of Japan open file report* **2005**, *419*, 285.

(28) Brookins, D. G. *Eh-pH diagrams for geochemistry*; Springer Science & Business Media, 2012.

(29) Zhang, D.; Wang, Z.; Liu, F.; Yi, P.; Peng, L.; Chen, Y.; Wei, L.; Li, H. Unraveling the pH-dependent oxygen reduction performance on single-atom catalysts: from single-to dual-sabatier optima. *J. Am. Chem. Soc.* **2024**, *146*, 3210–3219.

(30) Zhang, D.; Hirai, Y.; Nakamura, K.; Ito, K.; Matsuo, Y.; Ishibashi, K.; Hashimoto, Y.; Yabu, H.; Li, H. Benchmarking pH-field coupled microkinetic modeling against oxygen

reduction in large-scale Fe–azaphthalocyanine catalysts. *Chem. Sci.* **2024**, *15*, 5123–5132.

(31) Giannozzi, P.; Baroni, S.; Bonini, N.; Calandra, M.; Car, R.; Cavazzoni, C.; Ceresoli, D.; Chiarotti, G. L.; Cococcioni, M.; Dabo, I.; et al. QUANTUM ESPRESSO: a modular and open-source software project for quantumsimulations of materials. *J. Condens. Matter Phys.* **2009**, *21*, 395502.

(32) Fumagalli, L.; Esfandiar, A.; Fabregas, R.; Hu, S.; Ares, P.; Janardanan, A.; Yang, Q.; Radha, B.; Taniguchi, T.; Watanabe, K.; et al. Anomalously low dielectric constant of confined water. *Science* **2018**, *360*, 1339–1342.

(33) Trasatti, S.; Lust, E. *Modern aspects of electrochemistry*; Springer, 1999; pp 1–215.